CSMA 2026
17ème Colloque National en Calcul des Structures
18-22 Mai 2026, Presqu'île de Giens (Var)

FFT-based homogenization on boundary-conforming grids of finite elements

F. Bignonnet[1], M. Ladecký[2], I. Pultarová[3], J. Zeman[3]

[1] *Nantes Université, École Centrale Nantes, CNRS, GeM, UMR 6183, F-44600 Saint-Nazaire, France, francois.bignonnet@univ-nantes.fr*
[2] *Department of Microsystems Engineering, University of Freiburg, Freiburg, Germany, martin.ladecky@imtek.uni-freiburg.de*
[3] *Faculty of Civil Engineering, Czech Technical University in Prague, Prague, Czech Republic, ivana.pultarova@cvut.cz, jan.zeman@cvut.cz*

Résumé — Computational homogenization with fast Fourier transforms (FFT) is usually formulated on a uniform grid. The spatial convergence is here improved by transforming the grid into a boundary-conforming one. The mechanical problem is discretized using the finite element method (FEM), with isoparametric transformation of elements and application of the Green operator in the pulled-back configuration. Numerical investigations confirm that the homogenized properties and the local fields obtained on boundary-conforming grids have much faster spatial convergence than uniform grid ones.
Mots clés — Computational homogenization, Fast Fourier transform, Green operator, Finite element discretization, Grid adaptation

1 Introduction

The macroscopic mechanical properties of heterogeneous media can be determined by homogenization from the resolution of a boundary value problem defined on a Representative Volume Element (RVE) of the microstructure. Methods based on the Green operator and fast Fourier transform (FFT), pioneered by Moulinec & Suquet [10], have emerged as an efficient alternative to the finite element method (FEM) for computational homogenization (see reviews [11, 9]). These methods draw their efficiency from the combination of a matrix-free implementation, a cheap application of the Green operator in the Fourier space using FFT, and a favorable spectrum of eigenvalues of the discretized system of equations.

The spatial accuracy of early FFT-based methods suffered from both ringing artifacts due to the discretization on a trigonometric basis and a poor description of boundaries between constituents due to the uniform discretization grid. Ringing artifacts can be addressed by the use of alternative discretizations, such as finite differences or finite elements [12, 8].

Yet, in a uniform grid, elements usually fail to conform to material boundaries. This introduces a loss of accuracy near boundaries between material phases. In the case of a discontinuous and piecewise constant stiffness field on subdomains with C^2-smooth boundaries, first order Lagrange FEM with boundary-conforming elements yields h^1 convergence of the FEM solution u_h to the exact one u in H^2 norm, and h^2 convergence of the homogenized stiffness. If the mesh does not conform to the boundary, as for uniform grids, the rate of convergence of u_h to u can drop to $h^{1/2}$, and that of the homogenized stiffness to h^1 [1]. Further, using elements non conforming with material boundaries compromises the potential accuracy gains of higher-order FEM discretizations. To overcome these limitations, one solution is to enrich the discretization space at boundaries using X-FEM [6]. Another solution is to transform the uniform grid, as recently investigated for discretizations with finite differences or trigonometric basis [13, 2, 14].

The present contributions, which summarize and complement [3], are as follows :

1. Formulate the grid transformation in the classical framework of isoparametric FEM, with the Green operator and FFT applied in the pulled-back configuration ;
2. Investigate the spatial convergence of the numerical solution and the number of iterations of the linear solver, for uniform and boundary conforming grids.

2 FFT-based method with finite element discretization and isoparametric grid transformation

2.1 Homogenization problem in small strain linear elasticity

A periodic unit-cell $\Omega = [0, L_1] \times \cdots \times [0, L_d]$ of the material occupies the d-dimensional real space $\mathbb{R}^d$ (d = 2, 3), where $L_i > 0$ are the side lengths of Ω. Let $\mathcal{V} = \{\mathbf{u} \in H^1(\Omega) \mid \Omega - \text{periodic}, \overline{\mathbf{u}} = 0\}$ stand for the set of periodic, first-order vector fields with null average over the RVE Ω belonging to the first order Sobolev space $H^1(\Omega)$.

The weak formulation of the homogenization problem in small strain linear elasticity is

$$\text{find } \mathbf{u} \in \mathcal{V}, \text{ such that } \forall \mathbf{v} \in \mathcal{V}, \quad \int_\Omega \boldsymbol{\nabla}^{\text{sym}} \mathbf{v} : \mathbb{C} : (\mathbf{E} + \boldsymbol{\nabla}^{\text{sym}} \mathbf{u}) \, \mathrm{d}\mathbf{x} = 0. \tag{1}$$

In (1), $\mathbf{u}$ denotes the fluctuation displacement, $\mathbf{E}$ the macroscopic strain and $\mathbb{C}$ the stiffness. The microscopic strain is $\boldsymbol{\epsilon} = \mathbf{E} + \boldsymbol{\nabla}^{\text{sym}} \mathbf{u}$ and the microscopic stress is $\boldsymbol{\sigma} = \mathbb{C} : \boldsymbol{\epsilon}$. The homogenized stiffness $\mathbb{C}^{\text{hom}}$ relates the macroscopic stress $\overline{\boldsymbol{\sigma}}$ to the macroscopic strain $\mathbf{E} = \overline{\boldsymbol{\epsilon}}$ by $\overline{\boldsymbol{\sigma}} = \mathbb{C}^{\text{hom}} : \overline{\boldsymbol{\epsilon}}$, where the overbar denotes the volume average over Ω.

2.2 Finite element discretization on uniform grids

The unit cell Ω is decomposed in $N_p = N_1 \times \cdots \times N_d$ periodic reproductions $\mathcal{P}_{\mathtt{p}}$ of a reference pattern $\mathcal{P}_{\mathtt{0}}$. The Cartesian index $\mathtt{p} \in I(\mathtt{N}) = \{0 \dots N_1 - 1\} \times \cdots \times \{0 \dots N_d - 1\}$ denotes the pattern position in the grid. Each pattern $\mathcal{P}_{\mathtt{p}}$ contains N_e elements $\mathcal{E}^e_{\mathtt{p}}$ and N_q quadrature points $\mathbf{x}^q_{\mathtt{p}}$, where $e \in \{1, \dots, N_e\}$ and $q \in \{1, \dots, N_q\}$ are the element and quadrature point indices in the reference pattern. There are N_p nodes $\mathbf{x}^n_{\mathtt{p}}$, $N_p N_e$ elements and $N_p N_q$ quadrature points $\mathbf{x}^q_{\mathtt{p}}$ in the grid. The stride of the pattern, equivalent to pixel/voxel edge lengths, is $\mathbf{h}$ such that $h_i = L_i / N_i$.

Nodal values of the displacement $\mathbf{u}_{\mathtt{p}} = \mathbf{u}(\mathbf{x}^n_{\mathtt{p}})$ are assembled in a vector of degrees of freedom $\mathbf{u} = \{\mathbf{u}_{\mathtt{p}}\}_{\mathtt{p} \in I(\mathtt{N})}$ containing dN_p scalars. Periodic shifts $\mathtt{s} \in \{-1, 0, 1\}^d$ of Cartesian grid indices are introduced to refer to a pattern $\mathcal{P}_{\mathtt{p}+\mathtt{s}}$ adjacent to a pattern $\mathcal{P}_{\mathtt{p}}$. The sum $\mathtt{p} + \mathtt{s}$ must be understood periodically and element-wise, such that $\mathtt{p} + \mathtt{s} \in I(\mathtt{N})$. The nodes of an element $\mathcal{E}^e_{\mathtt{p}}$ are at positions $\mathbf{x}^n_{\mathtt{p}+\mathtt{s}}$, where shifts $\mathtt{s} \in \mathtt{S}^e \subset \{0, 1\}^d$. At a point $\mathbf{x}$ of an element $\mathcal{E}^e_{\mathtt{p}}$, displacements are interpolated from nodal values by interpolation functions $\phi^e_{\mathtt{s}}$ of the reference element $\mathcal{E}^e_{\mathtt{0}} \subset \mathcal{P}_{\mathtt{0}}$. For $\mathbf{y} = \mathbf{x} - \mathtt{p}\mathbf{h} \in \mathcal{E}^e_{\mathtt{0}}$, interpolation functions of $\phi^e_{\mathtt{s}}$ verify $\phi^e_{\mathtt{s}}(\mathbf{y}^n_{\mathtt{p}+\mathtt{r}}) = 1$ if $\mathtt{r} = \mathtt{s}$ else 0 for all shifts $\mathtt{r}, \mathtt{s} \in \mathtt{S}^e$. Hence displacements at a point $\mathbf{x}$ of an element $\mathcal{E}^e_{\mathtt{p}}$ are interpolated as :

$$\mathbf{u}(\mathbf{x}) = \sum_{\mathtt{s} \in \mathtt{S}^e} \mathbf{u}_{\mathtt{p}+\mathtt{s}} \phi^e_{\mathtt{s}}(\mathbf{y}) \quad \text{where} \quad \mathbf{y} = \mathbf{x} - \mathtt{p}\mathbf{h} \in \mathcal{E}^e_{\mathtt{0}}. \tag{2}$$

The gradient of displacement at quadrature points $\mathbf{x}^q_{\mathtt{p}}$ of an element $\mathcal{E}^e_{\mathtt{p}}$ is then

$$\boldsymbol{\nabla} \mathbf{u}^q_{\mathtt{p}} = \sum_{\mathtt{s} \in \mathtt{S}^e} \mathbf{u}_{\mathtt{p}+\mathtt{s}} \otimes \mathbf{B}^q_{\mathtt{s}} \quad \text{where} \quad \mathbf{B}^q_{\mathtt{s}} = \boldsymbol{\nabla} \phi^e_{\mathtt{s}}(\mathbf{y}^q). \tag{3}$$

All gradients at quadrature points are gathered in a vector $\boldsymbol{\nabla}\mathbf{u} = \{\boldsymbol{\nabla}\mathbf{u}^q_{\mathtt{p}}\}_{\mathtt{p} \in I(\mathtt{N}), q \in \{1, \dots, N_q\}}$ of size $d^2 N_p N_q$. The discrete gradient operator $\tilde{\mathbf{B}}$ of size $d^2 N_p N_q \times dN_p$, obtained by assembly of the $\mathbf{B}^q_{\mathtt{s}}$, is defined such that $\boldsymbol{\nabla}\mathbf{u} = \tilde{\mathbf{B}}\mathbf{u}$. Similarly, the operator $\mathbf{B}$ of size $d_* N_p N_q \times dN_p$ of the symmetric gradient, where $d_* = d(d+1)/2$, is such that $\boldsymbol{\nabla}^{\text{sym}} \mathbf{u} = \mathbf{B}\mathbf{u}$. After Gauss quadrature, the discretized weak form (1) becomes

$$\forall \mathbf{v} \in \mathbb{R}^{dN_p}, \mathbf{v}^T \mathbf{B}^T \mathbf{W} \mathbf{C} (\mathbf{E} + \mathbf{B}\mathbf{u}) = 0, \tag{4}$$

where $\mathbf{v}$ is the vector of nodal values of the test displacements, $\mathbf{C}$ and $\mathbf{W}$ are the $d_* N_p N_q \times d_* N_p N_q$ block-diagonal matrices containing the stiffness at quadrature points and quadrature weights, and $\mathbf{E}$ is the $d_* N_p N_q$ vector built from the uniform macroscopic strain $\mathbf{E}$. Equation (4) corresponds to the linear system

$$\mathbf{K}\mathbf{u} = \mathbf{f} \text{ where } \mathbf{K} = \mathbf{B}^T \mathbf{W} \mathbf{C} \mathbf{B} \text{ and } \mathbf{f} = -\mathbf{B}^T \mathbf{W} \mathbf{C} \mathbf{E} \tag{5}$$

In (5), $\mathbf{K}$ is the $dN_p \times dN_p$ stiffness matrix and $\mathbf{f}$ the vector of generalized forces due to the macroscopic strain.

2.3 Finite element discretization on transformed grids

Geometrical transformation of the grid To discretize the problem on a non uniform yet structured grid, two grids are now introduced. The uniform grid is transformed into a structured grid by the mapping $\mathbf{x} = \Phi(\tilde{\mathbf{x}}) = \tilde{\mathbf{x}} + \widetilde{\mathbf{u}_\Phi}(\tilde{\mathbf{x}})$ from the computational domain $\tilde{\Omega}$ to the physical domain Ω. The mapping displacement $\widetilde{\mathbf{u}_\Phi}(\tilde{\mathbf{x}})$ belongs to $H^1(\tilde{\Omega})$ and is $\tilde{\Omega}$-periodic. The fluctuation displacement $\mathbf{u}(\mathbf{x})$ in Ω is mapped from $\tilde{\Omega}$ by $\tilde{\mathbf{u}}(\tilde{\mathbf{x}}) = \mathbf{u}(\Phi(\tilde{\mathbf{x}}))$, where $\tilde{\mathbf{u}} \in \tilde{\mathcal{V}}$. The gradient of the displacement $\boldsymbol{\nabla}\mathbf{u} = \partial\mathbf{u}/\partial\mathbf{x}$ in the physical domain Ω is related to the gradient $\tilde{\boldsymbol{\nabla}}\tilde{\mathbf{u}} = \partial\tilde{\mathbf{u}}/\partial\tilde{\mathbf{x}}$ in the computational domain $\tilde{\Omega}$ by chain rule

$$\tilde{\boldsymbol{\nabla}}\tilde{\mathbf{u}} = \frac{\partial\tilde{\mathbf{u}}}{\partial\tilde{\mathbf{x}}} = \boldsymbol{\nabla}\mathbf{u}\cdot\mathbf{F} \quad \text{where} \quad \mathbf{F} = \tilde{\boldsymbol{\nabla}}\Phi \quad ; \quad J = \det(\mathbf{F}). \tag{6}$$

The weak formulation (1) of the homogenization problem in the physical domain Ω is pulled back to the computational domain $\tilde{\Omega}$:

$$\forall\tilde{\mathbf{v}} \in \tilde{\mathcal{V}}, \int_{\tilde{\Omega}} \mathrm{sym}(\tilde{\boldsymbol{\nabla}}\tilde{\mathbf{v}}\cdot\mathbf{F}^{-1}) : \mathbb{C} : (\mathbf{E} + \mathrm{sym}(\tilde{\boldsymbol{\nabla}}\tilde{\mathbf{u}}\cdot\mathbf{F}^{-1}))J\,\mathrm{d}\tilde{\mathbf{x}} = 0. \tag{7}$$

Isoparametric transformation We consider an isoparametric transformation of the elements of the uniform grid [5]. Each node $\tilde{\mathbf{x}}^n_{\mathtt{p}} \in \tilde{\Omega}$ of the uniform grid is transported at $\mathbf{x}^n_{\mathtt{p}} = \tilde{\mathbf{x}}^n_{\mathtt{p}} + \widetilde{\mathbf{u}_\Phi}(\tilde{\mathbf{x}}^n_{\mathtt{p}})$ in Ω. The periodic nodal mapping displacements are stored in a vector $\widetilde{\mathbf{u}_\Phi}$. A point $\tilde{\mathbf{x}}$ in the element $\mathcal{E}^e_{\mathtt{p}}$ is transported at $\mathbf{x}$ in the element $\mathcal{E}^e_{\mathtt{p}}$ by interpolation as in (2), and the fluctuation displacement $\mathbf{u}$ is interpolated from nodal values $\tilde{\mathbf{u}}$ in the computational grid as follows

$$\begin{aligned} \mathbf{x} = \tilde{\mathbf{x}} + \widetilde{\mathbf{u}_\Phi}(\tilde{\mathbf{x}}) \quad &= \tilde{\mathbf{x}} + \sum_{\mathtt{s}\in\mathbf{S}^e} (\widetilde{\mathbf{u}_\Phi})_{\mathtt{p}+\mathtt{s}}\,\phi^e_{\mathtt{s}}(\tilde{\mathbf{y}}) \\ \mathbf{u}(\mathbf{x}) = \tilde{\mathbf{u}}(\tilde{\mathbf{x}}) \quad &= \sum_{\mathtt{s}\in\mathbf{S}^e} \tilde{\mathbf{u}}_{\mathtt{p}+\mathtt{s}}\phi^e_{\mathtt{s}}(\tilde{\mathbf{y}}) \end{aligned} \qquad \text{where} \quad \tilde{\mathbf{y}} = \tilde{\mathbf{x}} - \mathtt{p}\mathbf{h} \in \tilde{\mathcal{E}}^e_{\mathtt{0}}. \tag{8}$$

The gradient of the displacement $\mathbf{u}$ at quadrature points $\mathbf{x}^q_{\mathtt{p}} = \tilde{\mathbf{x}}^q_{\mathtt{p}} + \widetilde{\mathbf{u}_\Phi}(\tilde{\mathbf{x}}^q_{\mathtt{p}})$ follows from (6) as

$$(\boldsymbol{\nabla}\mathbf{u})^q_{\mathtt{p}} = \tilde{\boldsymbol{\nabla}}\tilde{\mathbf{u}}^q_{\mathtt{p}} \cdot \left(\mathsf{F}^q_{\mathtt{p}}\right)^{-1} \quad \text{with} \quad \mathsf{F}^q_{\mathtt{p}} = \mathbf{I} + \left(\widetilde{\tilde{\boldsymbol{\nabla}}\widetilde{\mathbf{u}_\Phi}}\right)^q_{\mathtt{p}}, \tag{9}$$

where $\tilde{\boldsymbol{\nabla}}\tilde{\mathbf{u}} = \tilde{\mathsf{B}}\tilde{\mathbf{u}}$ and $\tilde{\boldsymbol{\nabla}}\widetilde{\mathbf{u}_\Phi} = \tilde{\mathsf{B}}\widetilde{\mathbf{u}_\Phi}$ from (3).

Transformed discrete problem The Gauss quadrature approximation of the pulled-back weak formulation (7) leads, as in (4), to the discretization of the homogenization problem (1) on a transformed grid

$$\tilde{\mathsf{K}}\tilde{\mathbf{u}} = \tilde{\mathbf{f}} \quad \text{where} \quad \tilde{\mathsf{K}} = \tilde{\mathsf{B}}^{\mathsf{T}}\tilde{\mathsf{W}}\tilde{\mathsf{C}}\tilde{\mathsf{B}} \text{ and } \tilde{\mathbf{f}} = -\tilde{\mathsf{B}}^{\mathsf{T}}\tilde{\mathsf{W}}\tilde{\mathsf{C}}\tilde{\mathsf{E}}, \tag{10}$$

where $\tilde{\mathsf{W}}$ is the $d^2N_pN_q \times d^2N_pN_q$ diagonal matrix built from the quadrature weights of the uniform grid. Note that a quadrature approximation which is exact on the uniform grid (for example $N_q = 4$ on a bilinear quadrilateral element) can result in an inexact integration on the transformed grid.

In (10), $\tilde{\mathsf{C}}$ is the $d^2N_pN_q \times d^2N_pN_q$ block diagonal matrix built from the pulled-back stiffness tensor $\tilde{\mathbb{C}}$ defined as [2] :

$$\tilde{C}_{ijk\ell} = JF^{-1}_{jp}C_{pikq}F^{-T}_{q\ell}, \tag{11}$$

where $\mathbf{F}$ and $J = \det(\mathbf{F})$ are obtained at each Gauss integration point as in (9). The fourth order tensor $\tilde{\mathbb{C}}$ is positive definite, possesses the major symmetry but not the minor symmetries.

The r.h.s. is formally constructed in (10) from the pulled-back stiffness and the pulled-back macroscopic strain $\tilde{\mathbf{E}}$ defined at quadrature points as the second order tensor $\tilde{\mathbf{E}}^q_{\mathtt{p}} = \mathbf{E}\cdot\mathsf{F}^q_{\mathtt{p}}$. The strain $\tilde{\mathbf{E}}$ is neither symmetric nor uniform. In practice, the explicit computation and storage of $\tilde{\mathsf{B}}$, $\tilde{\mathsf{C}}$, $\tilde{\mathsf{W}}$ and $\tilde{\mathbf{E}}$ are avoided by using an operator based implementation, see [3].

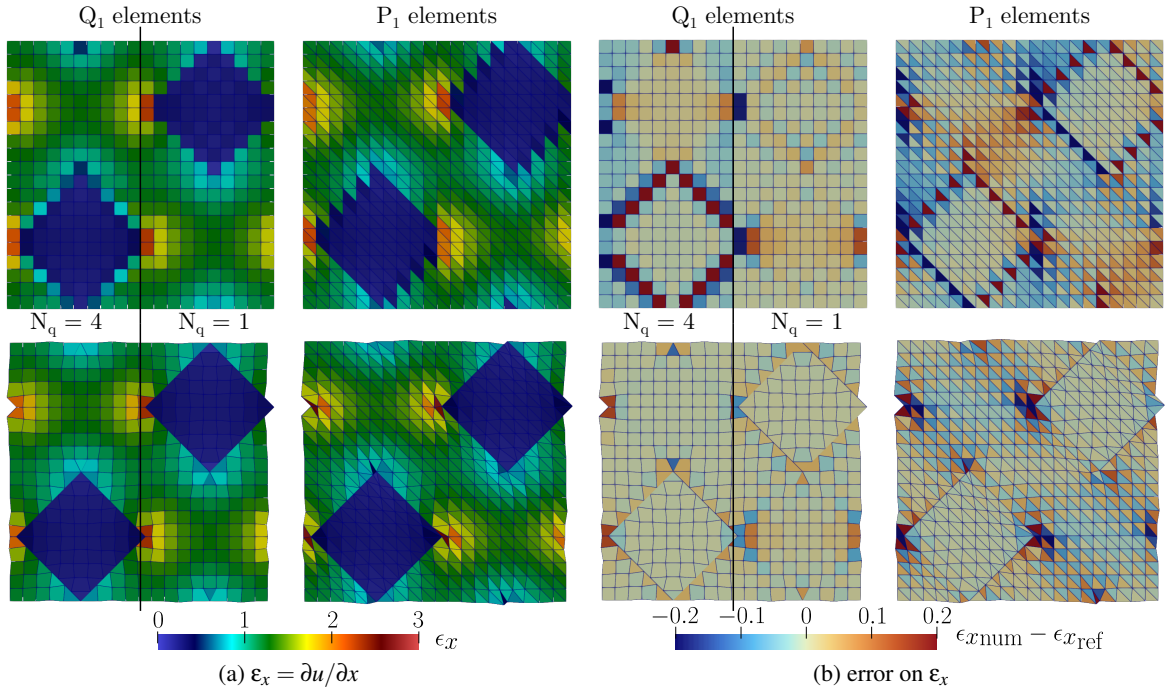

(a) $\varepsilon_x = \partial u/\partial x$ (b) error on ε_x

FIGURE 1 – Temperature gradient field for the diamond inclusion case on 20^2 uniform (top) or transformed (bottom) grids.

2.4 Resolution by preconditioned conjugate gradient with Green preconditioner

The linear system (10) is symmetric and positive, semi-definite. It is efficiently solved using the preconditioned conjugate gradient (PCG). However, the condition number of the stiffness matrix $\mathbf{K}$ or $\tilde{\mathbf{K}}$ deteriorates significantly as the grid size is increased.

In FFT-based methods, the application of the Green operator can be interpreted as a geometrically optimal preconditioner [8]. Namely, a reference stiffness matrix $\mathbf{K}_0$ is defined on the uniform grid as in (5), where the heterogeneous stiffness field $\mathbb{C}$ is replaced by a homogeneous reference stiffness $\mathbb{C}_0$. The matrix $\mathbf{K}_0$ is circulant, and its discrete Fourier transform is block-diagonal [8, 3]. As a result, its pseudo-inverse, referred to as the Green operator $\mathbf{G}_0$, can be efficiently applied in the Fourier space.

The resolution of the linear system (10) by PCG with preconditioner $\mathbf{K}_0$ is equivalent to the resolution of the system $\mathbf{G}_0\tilde{\mathbf{K}}\tilde{\mathbf{u}} = \mathbf{G}_0\tilde{\mathbf{f}}$ by conjugate gradient. The spectrum of eigenvalues of the matrix $\mathbf{G}_0\tilde{\mathbf{K}}$ can be bounded from the local eigenvalues of $\mathbb{C}_0^{-1} : \tilde{\mathbb{C}}$ [8]. As a result, at least for uniform grids, the bounds on the condition number of the preconditioned system do not deteriorate as the grid size is increased. However, the transformation gradient $\mathbf{F}$ of the grid, involved in $\tilde{\mathbb{C}}$ (11), can deteriorate the spectrum of eigenvalues of the preconditioned system as compared to the one obtained on a uniform grid.

3 Numerical investigations

3.1 Test cases and numerical set up

Three two-dimensional test cases ($d = 2$) are investigated. The first consists in diamond inclusions, for a heat conductivity problem. The second is Hashin's composite inclusion, and the third comprises randomly positioned, non-overlapping disks, both in plane strain elasticity. The two first cases benefit from analytical solutions. Three dimensional test cases investigated in [3] lead to similar conclusions.

Diamond inclusions The diamond inclusion case (see Fig. 1) consists in two diamonds, or squares inclined at 45 degree w.r.t. to the discretization grid. Squares are positioned on an inclined checkerboard pattern, to benefit from the analytical solution provided in [4]. The conductivity of the diamond inclusions is $10\mathbf{I}$ and that of the matrix and the reference medium is $\mathbf{I}$. The macroscopic temperature gradient is set to $\overline{\boldsymbol{\nabla} u} = \mathbf{e}_x$.

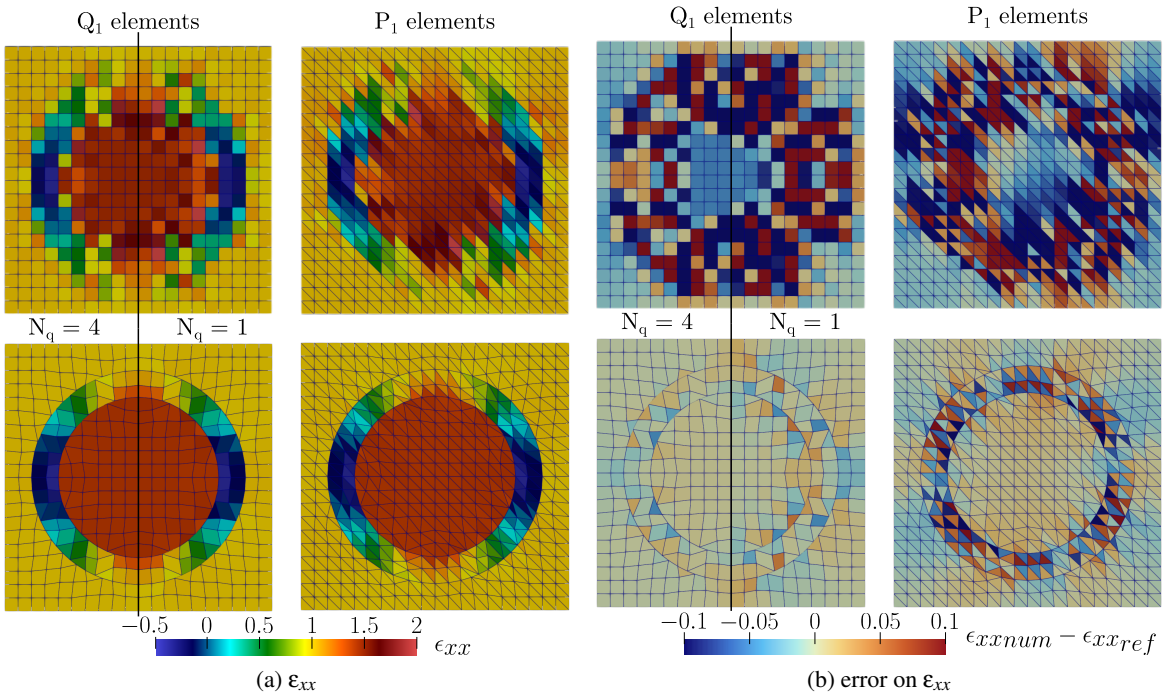

(a) ε_{xx} (b) error on ε_{xx}

FIGURE 2 – Strain field for the composite inclusion case on 20^2 uniform (top) or transformed (bottom) grids.

Hashin's composite inclusion Hashin's composite inclusion [7] (see Fig. 2) consists in a composite cylinder with a soft core and a stiff shell, surrounded by a matrix. The inclusion core ($i=1$), shell ($i=2$) and the matrix ($i=3$) have uniform isotropic stiffness $\mathbb{C}_i$ with Lamé parameters λ_i, μ_i and bulk modulus $\kappa_i = \lambda_i + 2\mu_i/d$. The core radius is $R_1 = 0.3$, shell radius $R_2 = 0.4$ and unit cell edge length 1. A plane isotropic load $\mathbf{E} = \mathbf{I}_{2d}$ is applied. The composite inclusion is neutral provided the matrix bulk modulus κ_3 is set to the equivalent bulk modulus of the inclusion $\kappa^{\text{hom}} = \kappa_2[1 - d\alpha\phi/(1+\alpha\phi)]$ where $\phi = (R_1/R_2)^d$ and $\alpha = d(\kappa_2 - \kappa_1)/[(d-1)2\mu_2 + d\kappa_1]$. In that case, $\boldsymbol{\epsilon} = \mathbf{I}_{2d}$ in the matrix and $(1+\alpha)/(1+\alpha\phi)\mathbf{I}_{2d}$ in the core. The shell moduli are set to $\lambda_2 = 1, \mu_2 = 0.5$ and the core stiffness to $\mathbb{C}_1 = 0.1\mathbb{C}_2$. The matrix bulk modulus κ_3 is set to κ^{hom}, and its shear modulus μ_3 set such that $\mathbb{C}_3$ is a scalar multiple of $\mathbb{C}_2$. The reference stiffness is $\mathbb{C}_0 = \mathbb{C}_2$.

Random disks The last case consists in 25 non overlapping disks of radius $R = 0.05$, which are positioned by a random sorption algorithm in a unit cell of side length 1 (see Fig. 3). The matrix moduli are set to $\lambda_2 = 1, \mu_2 = 0.5$, the inclusion stiffness to $\mathbb{C}_1 = 0.01\mathbb{C}_2$ and the reference stiffness to $\mathbb{C}_0 = \mathbb{C}_2$. The macroscopic strain is set to $\mathbf{e}_x \otimes \mathbf{e}_x$.

Discretization The diamond and composite inclusion cases are discretized on grids from 20^2 to 2560^2 nodes, and the random inclusion cases on grids from 40^2 to 2560^2 nodes. Three types of patterns are considered : one bilinear quadrangular Q_1 element with either $N_q = 1$ or 4 quadrature points, or two linear triangular P_1 elements, each with one quadrature point, for a total of $N_q = 2$ quadrature point per pattern. Strain is evaluated only at the center of mass of the elements during the post-processing.

Grid adaptation The grid adaptation is performed as follows. First, all patterns are labeled to belong to a material phase depending on the position of their center. Then, nodes belonging to adjacent elements with different labels are defined as boundary nodes. These nodes are orthogonally projected on the actual nearest boundary. If two boundary nodes become too close after projection, generating excessively flat elements, they are relocated. After this step, some nodes adjacent to boundary nodes may be too close to boundary nodes. The grid is thus relaxed by setting the mapping displacement of all non-boundary nodes equal to $1/3$ of the sum of mapping displacements of the 3^d nodes of adjacent patterns.

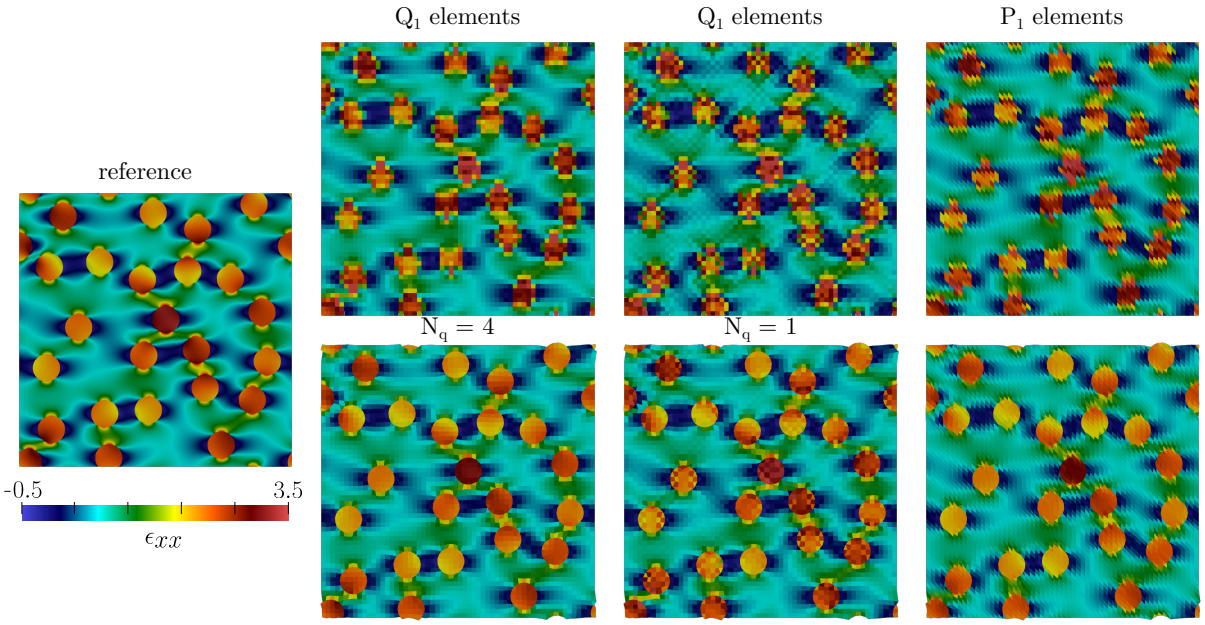

FIGURE 3 – Strain field for the random inclusion case on 60^2 uniform (top) or transformed (bottom) grids. Reference is obtained on a transformed 1280^2 grid of Q_1 elements with $N_q = 4$.

3.2 Quality of solution fields and spatial convergence

Fields of the temperature gradient or strain of the numerical solution are shown in Figs. 1, 2 and 3. For the three cases and the three types of discretization, the boundary-conforming grid adaptation systematically leads to a strong improvement in the quality of the fields. Large errors at material boundaries obtained on low resolution uniform grids are cured by the grid adaptation. The Q_1 elements with reduced integration ($N_q = 1$) are known to introduce hourglassing of the solution fields on uniform grids. This hourglassing manifests much less on transformed grids, at the exception of the strain in the very soft random inclusions. Patterns with Q_1 elements and $N_q = 4$ quadrature points visually lead to the most accurate solution fields.

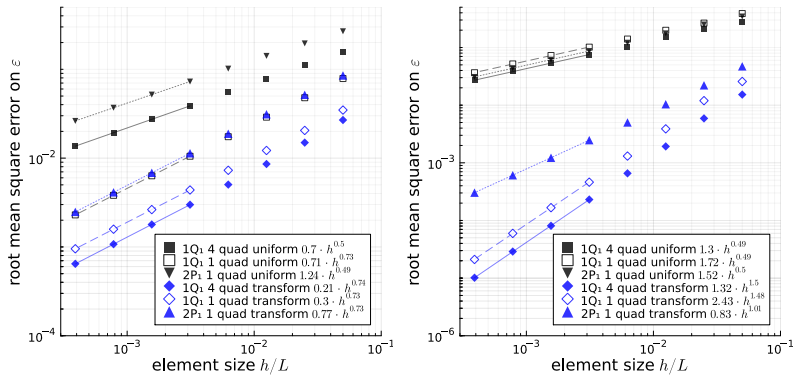

(a) diamond inclusions (b) composite inclusion

FIGURE 4 – Root mean square error (RMSE) on temperature gradient (a) or strain (b) fields.

These qualitative observations are confirmed by quantifying the root mean square error of the solution fields as compared to the exact solutions for the diamond and composite inclusion cases, see Fig. 4. Temperature gradient or strain fields obtained on uniform grids show a $h^{1/2}$ spatial convergence, as expected from [1]. In turn, the temperature gradient in the diamond inclusion case shows a $h^{3/4}$ convergence, while the strain field in the composite inclusion case shows at least a h^1 convergence. Indeed, the solution to the diamond inclusion case is not smooth enough due to a singularity at the diamond tips, while the solution to the composite inclusion has sufficient smoothness.

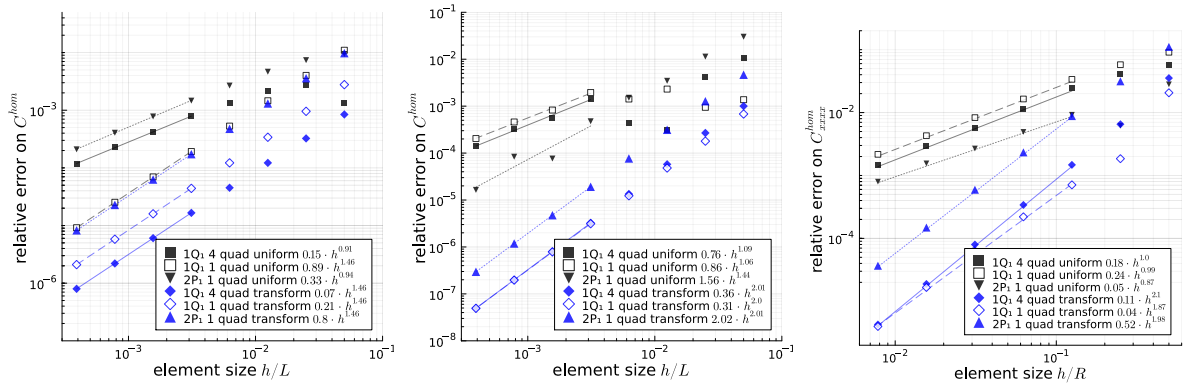

(a) diamond inclusions $\mathbf{C}^{\text{hom}}_{xx}$ (b) composite inclusion $\mathbb{C}^{\text{hom}}_{xxxx}$ (c) random inclusions $\mathbb{C}^{\text{hom}}_{xxxx}$

FIGURE 5 – Relative error on the homogenized conductivity (a) or stiffness (b,c).

Similarly, the spatial convergence of the homogenized conductivity or stiffness is shown in Fig. 5. The exact stiffness is not known for the random inclusion case, but a reference value is determined by extrapolation of results on several fine grids to the limit $h/R \to 0$. Homogenized properties obtained on uniform grids show a h^1 spatial convergence, while those on uniform grids show a h^2 convergence for the composite and random inclusion cases. These rates are expected from [1] for sufficiently smooth exact solutions. For the diamond inclusion case, with non smooth material boundaries, the rate drops to roughly $h^{3/2}$.

In all cases, the boundary-conforming grid adaptation leads to a significant reduction in the errors. On boundary-conforming grids, quadrangular bilinear Q_1 elements appear to perform better than triangular P_1 elements for the three investigated test cases.

3.3 Influence of grid adaption on the number of iterations of the linear solver

The grid adaptation comes at a price : the eigenvalue spectrum of the preconditioned operator is usually less favorable on a transformed grid than on a uniform one [2, 3]. Fig. 6 shows the number of iterations of the preconditioned conjugate gradient (PCG) required to reach a tolerance of 10^{-10} on the relative norm of residual (w.r.t. to that of the r.h.s.) in preconditioner norm.

On uniform grids, the number of iterations shows mesh insensitivity as the grid size is increased. The mesh insensitivity results from the preconditioning by the Green operator [8], and is one of the greatest asset of FFT-based methods. As the grid is transformed, the number of iterations of PCG is increased by a factor 2 for the diamond inclusion case, a factor 3 for the composite inclusion one and nearly a factor 4 for the random inclusion case. It shows a mild sensitivity to the grid size.

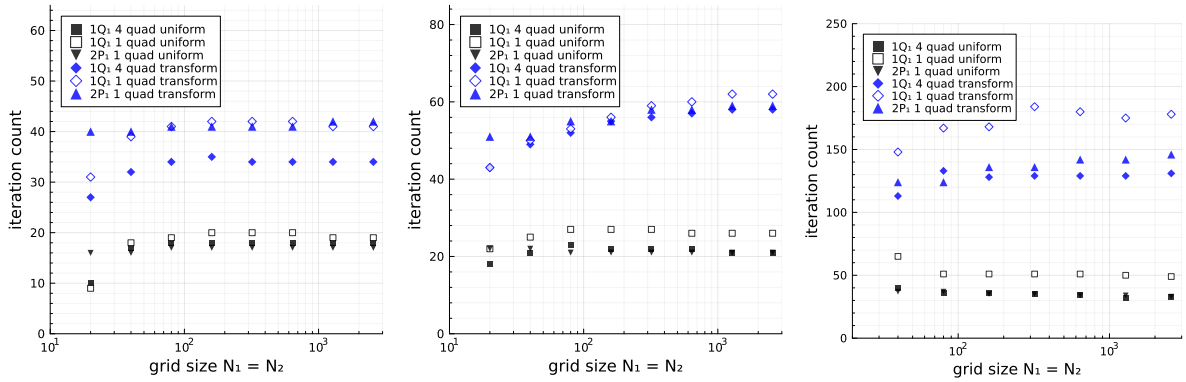

(a) diamond inclusions (b) composite inclusion (c) random inclusions

FIGURE 6 – Number of iterations of the preconditioned conjugate gradient.

4 Conclusion

The technique of grid adaptation for FFT-based methods is here formulated for a FE discretization using the well established formalism of isoparametric transformation of elements. The numerical scheme can be efficiently implemented using a matrix free, operator-based implementation [3]. The Green operator is used as a preconditioner in the pulled-back computational grid. The linear system is efficiently solved using the preconditioned conjugate gradient (PCG).

Through a series of numerical experiments, we show that transforming the discretization grid to conform to material boundaries leads to a strong increase in the quality of the solution fields. Convergence estimates for uniform or boundary-conforming meshes are retrieved : provided the exact solution is smooth enough, a boundary-conforming grid adaptation can shift the rate of spatial convergence of the numerical solution strain to the exact one from $h^{1/2}$ to h, and that of the homogenized stiffness from h to h^2. In the mean time, the number of iteration for convergence of the PCG is increased by a factor 2 to 4 when the grid is adapted, and remains almost independent on the grid resolution. Overall, the computational overhead brought by grid adaptation is moderate, while the gain in accuracy is large.

Acknowledgments

FB acknowledges funding by Nantes Université for a semester as a visiting professor at Czech Technical University in Prague, and by l'Agence Nationale de la Recherche (ANR), project ANR-23-CE08-0036 (MOCAMOR). ML acknowledges funding by the European Commission (Marie Skłodowska-Curie Fellowship 101106585 — microFFTTO), and Cluster of Excellence livMatS. IP and JZ acknowledge funding by the European Union under the project ROBOPROX (reg. no. CZ.02.01.01/00/22_008/0004590).

Références

[1] I. Babuška. The finite element method for elliptic equations with discontinuous coefficients. *Computing*, 5(3) :207–213, Sep 1970.

[2] C. Bellis and R. Ferrier. Numerical homogenization by an adaptive fourier spectral method on non-uniform grids using optimal transport. *Computer Methods in Applied Mechanics and Engineering*, 419 :116658, 2024.

[3] F. Bignonnet, M. Ladecký, I. Pultarová, and J. Zeman. Fourier-based computational micromechanics on boundary-conforming transformed grids. Submitted to Comptes Rendus. Mécanique, 2025.

[4] R. V. Craster and Y. V. Obnosov. Four-phase checkerboard composites. *SIAM Journal on Applied Mathematics*, 61(6) :1839–1856, 2001.

[5] A. Ern and J.-L. Guermond. *Theory and Practice of Finite Elements*. Springer New York, NY, 2004.

[6] F. Gehrig and M. Schneider. An X-FFT solver for two-dimensional thermal homogenization problems. *International Journal for Numerical Methods in Engineering*, 126(7) :e70022, 2025.

[7] Z. Hashin. The elastic moduli of heterogeneous materials. *Journal of Applied Mechanics*, 29(1) :143–150, 03 1962.

[8] M. Ladecký, R. J. Leute, A. Falsafi, I. Pultarová, L. Pastewka, T. Junge, and J. Zeman. An optimal preconditioned FFT-accelerated finite element solver for homogenization. *Applied Mathematics and Computation*, 446 :127835, 2023.

[9] S. Lucarini, M. Upadhyay, and J. Segurado. Fft based approaches in micromechanics : fundamentals, methods and applications. *Modelling and Simulation in Materials Science and Engineering*, 30(2) :023002, 2021.

[10] H. Moulinec and P. Suquet. A fast numerical method for computing the linear and non linear properties of composites. *Comptes Rendus de l'Académie des Sciences*, 2(318) :1417–1423, 1994.

[11] M. Schneider. A review of nonlinear FFT-based computational homogenization methods. *Acta Mechanica*, 232(6) :2051–2010, 2021.

[12] M. Schneider, D. Merkert, and M. Kabel. FFT-based homogenization for microstructures discretized by linear hexahedral elements. *International Journal for Numerical Methods in Engineering*, 109(10) :1461–1489, 2017.

[13] M. Zecevic, R. A. Lebensohn, and L. Capolungo. New large-strain FFT-based formulation and its application to model strain localization in nano-metallic laminates and other strongly anisotropic crystalline materials. *Mechanics of Materials*, 166 :104208, 2022.

[14] M. Zecevic, R. A. Lebensohn, and L. Capolungo. Achieving geometric accuracy in FFT-based micromechanical models using conformal grid. *Mechanics of Materials*, 212 :105512, 2026.